Environmental Science & Technology

pubs.acs.org/est

Article

Fate and Transport of Pharmaceuticals in Iron and Manganese Binary Oxide Coated Sand Columns

Tao Luo, Rasesh Pokharel, Tao Chen, Jean-François Boily, and Khalil Hanna*

Cite This: *Environ. Sci. Technol.* 2023, 57, 214−221

Read Online

ACCESS | Metrics & More | Article Recommendations | Supporting Information

ABSTRACT: Predicting the fate and transport of pharmaceuticals in terrestrial environments requires knowledge of their interactions with complex mineral assemblages. To advance knowledge along this front, we examined the reactivity of pipemidic acid (PIP), a typical quinolone antibiotic, with quartz particles coated with a mixture of manganese oxide (MnO_2) and goethite (α-FeOOH) under static and dynamic flow conditions. Batch and dynamic column experiments showed that PIP binding to MnO_2 proceeded through a heterogeneous redox reaction, while binding to goethite was not redox-reactive. Mixed columns of aggregated goethite-manganese particles however enhanced redox reactivity because (i) goethite facilitated the transport of dissolved Mn(II) ion and increased the retention of PIP oxidation products, and (ii) MnO_2 was protected from passivation. This mobility behavior was predicted using transport models accounting for adsorption and transformation kinetics of PIP on both goethite and MnO_2. This work sheds new light on reactivity changes of mixtures of Fe and Mn oxides under flow-through conditions and will have important implications in predicting the fate and transport of redox-active organic compounds as well as development of new geomedia filters for environmental remediation.

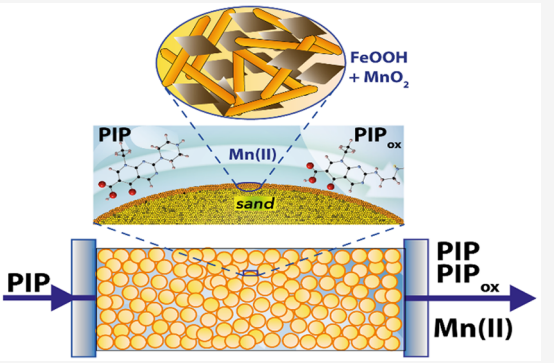

KEYWORDS: *pharmaceuticals, goethite, manganese oxide, redox, geomedia filter, transport, modeling*

INTRODUCTION

Iron (Fe) and manganese (Mn) are the two most common redox-active elements in the Earth's crust. They are present in a wide range of environments with different composition, mineralogy, and morphology.[1,2] For example, Fe- and Mn-oxides may coexist with each other as discrete particles, a mixture of component phases, or particulate coatings in soils and sediments.[3] In deep sea waters, Mn and Fe are oxidized to form ferromanganese crusts and nodules on the oceans floor, a mineral of immense economic interest. Because of their specific nanoscale properties, high surface area, low cost, strong oxidation, and sorption abilities, iron and manganese oxides are widely used in various environmental applications.[4−8] They play a key role in controlling the fate and mobility of elements and toxic compounds in nature and can also be used as an environmentally friendly geomedia filter in water treatment technologies and/or aquifer recharge management.[9−11]

Goethite (α-FeOOH) is one of the most thermodynamically stable iron oxyhydroxides under ambient conditions and the most abundant one in natural settings.[2,12] For this reason, numerous theoretical and experimental studies explored organic or inorganic compound binding mechanisms to goethite surfaces and their impact on migration in nature.[13,14] Birnessite-type layered manganese oxides are, at the same time, of great interest given their strong redox- and cation-exchange reactivity.[8,15,16] Their interest is also motivated by their structural similarity to the biogenically precipitated natural manganese oxides, which are the most commonly occurring forms of MnO_2 in surficial environments.[1]

Although the reactivity of each individual or single phase has been widely investigated,[7,17−21] knowledge is limited on how binary mixtures of these two phases, goethite and MnO_2, alter the overall reactivity of environmental compounds. Previous studies[22−24] have reported that binary mixtures of $Fe(OH)_3$ with $Al(OH)_3$ or $SiO_{2(am)}$ have exhibited different adsorption properties from their component parts due to changes in surface site availability and surface charge. This has been ascribed to the dissolution of $Al(OH)_3$ or $SiO_{2(am)}$ and sorption/precipitation of the dissolved ions at Fe-oxides surfaces. Other studies[25] have reported that mixtures of MnO_2 with other oxides like Al_2O_3 or $SiO_{2(am)}$ or TiO_2 inhibited MnO_2 reactivity mainly through heteroaggregation between particles and/or adsorption of metal ions released from the second oxides on the MnO_2 surface. Two recent studies[26,27] even showed that Fe oxides inhibited MnO_2

Received: August 18, 2022
Revised: November 18, 2022
Accepted: November 21, 2022
Published: December 5, 2022

reactivity through heteroaggregation of positively charged Fe oxides particles with negatively charged MnO_2 particles, thereby reducing the number of surface sites of MnO_2. However, little is known on how this reactivity is affected under dynamic, flow-through conditions that are far more prevalent in environmental and/or engineered systems than the static (batch) modes more commonly employed in laboratory studies. This is particularly relevant because dissolved ions and/or redox byproducts (e.g., dissolved Mn(II)) concurrently affect surface reactivity of manganese and iron oxides minerals and the mobility of target compounds. As such, experimental work under continuous flow conditions can better emulate natural environments (e.g., geochemical systems containing Fe- and Mn-oxides) or engineered infiltration systems (e.g., managed aquifer recharge (MAR) and water treatment systems), where the target pollutants and the generated reaction products travel through and are then flushed out of the column system. In addition, most traditional environmental models are based on a single phase or simple system, and little is known about the redox reactivity within complex mineral assemblages. Knowledge of the adsorption and redox reactions that take place in the mixed mineral phases or complex environmental systems and under flow-through conditions is consequently needed to explore contaminant transport.

This study aims to assess the roles that coexisting iron and manganese oxides play on the fate and transport of contaminants under conditions of water flow. This was achieved by working with columns packed with sand microparticles (CS) coated with MnO_2 (MCS), goethite (GCS), or mixed goethite-MnO_2 (MGCS). Pipemidic acid (PIP) was, in turn, chosen as a representative redox-active quinolone antibiotic widely used in human and veterinary medicine[28] and commonly found in ng/L to μg/L levels[29−31] in aquatic environments and agricultural settings.[32−34] Investigation of redox transformation of compounds associated with reactive minerals is also required for an accurate assessment of ecological impacts of quinolone antibiotics. As the redox reaction is strongly dependent on the pH value and MnO_2/compound ratio, dynamic flow experiments of PIP were performed with two different MnO_2 amounts in the MGCS system and at pH 5.2 and 7.0, which are within the typical pH range for shallow groundwater and soil pore waters.[35] A transport model that accounts for adsorption and oxidation kinetics was used to predict changes in PIP transport in coated sands under flow. This work additionally explains how goethite-MnO_2 interactions affect PIP reactivity, and potentially how these mechanisms affect other similar environmental emerging contaminants.

2. MATERIALS AND METHODS

2.1. Synthesis of Minerals and Coated Phases. Pure Fontainebleau quartz sand (200−300 μm; ≤0.06 m^2/g) was chosen as an inert support, due to its very low reactivity and aqueous solubility under our experimental conditions.[36] The quartz sand was cleaned with HCl, H_2O_2, and ultrapure water to remove any colloidal or amorphous silica particles and organic/inorganic contaminants (see the SI for the detailed cleaning procedure). Acid birnessite (MnO_2) prepared according to McKenzie[37] was coated on quartz sand (MCS) as in our previous study[17] and summarized in the SI. Likewise, goethite (α-FeOOH) and goethite-coated quartz sand (GCS) were synthesized as described in previous studies[18,38−40] and summarized in the SI. The B.E.T. specific surface area of uncoated goethite and birnessite phases was 81 ± 4 and 65 ± 1 $m^2\ g^{-1}$, respectively, and the point of zero charge (PZC) determined at 298 K in 0.01, 0.1, and 1 M NaCl solutions by the potentiometric titration method was pH 9.1 for goethite and 2.4 for birnessite. Coating coverage was thereafter evaluated by total Mn and Fe concentrations of acid digested MCS and GCS. Concentrations, measured by Inductively Coupled Plasma-atomic Emission Spectrometry (ICP-AES), revealed 0.60 ± 0.02 (SD) mg Mn per 1 g of MCS and 6.2 mg ± 0.20 (SD) Fe per 1 g of GCS. These coating amounts are within the previously reported range for natural coated subsurface materials,[35,41] and they allow stable coated minerals to be achieved.

The possible dissolution of the used quartz sand was additionally checked in 1 and 10 g/L sand suspensions that were continuously stirred over a range of pH values (4−10) in pure water or 0.01 M NaCl for up to one month. In all cases, the dissolved silicate concentrations were below the detection limit of the molybdenum blue spectrophotometric method (<1 μM) and ICP-AES (<0.2 μM).

Binary mixtures of iron and manganese oxides (MGCS) were prepared by adding different amounts of MnO_2 suspension to GCS. Small aliquots of MnO_2 suspension were pipetted homogeneously over the GCS surface, then mixed with a polypropylene spatula, and dried overnight at room temperature. The resulting solid was thereafter washed four times with 10 mM NaCl to remove any uncoated MnO_2 and then dried again at room temperature. Two different MGCSs were prepared: 1) 0.05 MGCS and 2) 0.1 MGCS, where 0.05 and 0.1 indicate the percentage of MnO_2 in the MGCS system.

The Mn content in the MGCS was determined by dissolving in 30 mM ascorbic acid following the protocol of Charbonnet et al.[42] and analyzed by ICP/AES. The measured amount was 0.29 ± 0.02 (SD) mg of Mn in 1 g of 0.05 MGCS and 0.60 ± 0.02 (SD) mg of Mn in 1 g of 0.1 MGCS. Scanning electron microscopy (SEM) was applied to study the surface morphology of the MGCS matrix. Samples were examined with a JSM JEOL 7100 F microscope with a field emission gun and an OXFORD Genesis energy-dispersive X-ray spectrometer at 20 kV at a working distance of 5−10 mm and magnifications from 15000× to 30000×. SEM images of MGCS showed a mixture of goethite and MnO_2 particles deposited on the sand (Figure S1). Due to the extremely low Mn amount in the MGCS, X-ray diffraction could not be used for MGCS characterization.

2.2. Batch and Column Experiments. Three different sets of batch experiments were conducted to determine the 1) pH dependent adsorption of PIP on GCS with or without Mn(II), 2) pH dependent Mn(II) adsorption on GCS with or without PIP, 3) kinetics of PIP removal on 0.05 MGCS at pH 5.2, and 4) kinetic Mn(II) sorption on MCS and MGCS at pH 5.2 under static conditions. Details on the experimental setup are provided in the SI.

Dynamic breakthrough experiments were conducted at room temperature and under water-saturated conditions. Briefly, 15 g of GCS, MCS, or MGCS was packed in glass columns with an internal diameter of 1.6 cm and a bed length of 4.7 cm. The column was wrapped with aluminum foil to avoid any photoinduced degradation. The bulk density of the packed MGCS was 1.52 ± 0.05 g/cm^3, and the column pore volume (PV or V_p) was 4 ± 0.1 mL. The column was first saturated with a background solution of 10 mM NaCl

https://doi.org/10.1021/acs.est.2c05963
Environ. Sci. Technol. 2023, 57, 214−221

(previously purged with N_2) at pH 5.2 or 7.0 (depending on the experimental pH) with a constant flow rate of 0.5 mL/min (residence time of 8 min). A bromide tracer experiment was performed using an input solution containing 10 mM NaBr in 10 mM NaCl at pH 5.2 or 7.0. Br^- breakthrough curves for different columns (GCS, MCS, 0.05 MGCS, 0.1 MGCS) were obtained by analysis of the effluent solution using ion chromatography (Figure S2).

Different column experiments were performed by injecting input solutions consisting of a constant amount of 10 mM NaCl and 10 μM PIP but at two different pH values, 5.2 ($\pm$0.1) or 7.0 ($\pm$0.1). The investigated inflow concentration of PIP may appear higher than the level amounts of pharmaceuticals commonly detected in environmental systems[29−31] but close to a total dose of organic compounds found in industrial effluents or urban stormwater and municipal wastewater used in aquifer recharge.[42] Furthermore, since the Mn-based redox reaction is strongly dependent on the red/ox ratio, different MnO_2 amounts and thus different PIP/MnO_2 ratios were investigated. The experimental flow-rate was constant throughout the course of the experiment at 0.5 mL/min. The input solution was purged with N_2 to avoid CO_2 contamination and to maintain the experimental pH throughout the course of the experiment. The flow interruption method was applied in selected experiments to check the occurrence of kinetic limitations. All effluent solutions were collected using a fractional collector. The pH of the effluent solution was determined through the experiment by using an online pH meter. The effluent solution was also analyzed for PIP and byproducts with high-performance liquid chromatography (HPLC) and an ultrahigh-performance liquid chromatography−tandem mass spectrometry (UPLC-MS/MS) system and for dissolved metal ions using ICP-AES. More details about experimental conditions and measurements are reported in the SI (Table S1).

2.4. Transport Modeling. First, the hydrodynamic parameters were obtained by fitting the bromide breakthrough data using the classical Advection Dispersion Equation (ADE):

$$\frac{\partial C}{\partial t} = D\frac{\partial^2 C}{\partial x^2} - v\frac{\partial C}{\partial x} \tag{1}$$

Breakthrough curves (BTCs) for Br^- suggest the absence of great dispersion/diffusion or the physical nonequilibrium effect (Figure S2 in the SI). Macroscopic dispersivity (~1.89 mm) was obtained by the ratio of the dispersion coefficient (D) and pore velocity (v). Molecular diffusion was considered negligible with respect to the dynamic dispersion. The Péclet number (Pe = vL/D) was ~25 in the column, suggesting the predominance of a convective regime, and the flow can be assumed to be homogeneous. During water saturation and tracer experiments, total dissolved Mn, Fe, and Si in the outflow were below the ICP-AES detection limit (0.1 μM for Mn, 0.2 μM for Fe, and 0.2 μM of Si), and therefore, the possibility of mobilization and/or dissolution of minerals can be excluded. Blank tests conducted also confirmed no adsorption of Mn(II) ions to the quartz sand ($\leq$0.06 m^2/g).

The reactive transport model is based on a two-site, advective-dispersive transport model with degradation and Freundlich-Langmuir kinetic sorption. The liquid and sorbed concentrations are ruled by the following differential equation that governs the chemical nonequilibrium transport for a homogeneous system under steady-state water flow[43,44]

$$\frac{\partial C}{\partial t} + \frac{\rho \partial (S)}{\theta \partial t} = D\frac{\partial^2 C}{\partial x^2} - v\frac{\partial C}{\partial x} - \mu_1 C - \frac{\rho}{\theta}\mu_s S \tag{2}$$

where θ is the volumetric water content (L^3/L^3), C is the volume-averaged solution concentration (M/L^3), t is time (T), ρ is solid bulk density, S is the sorbed concentration (M/M), D is the dispersion coefficient in the liquid phase (L^2/T), v is the water velocity (L/T), and μ_l and μ_s are first-order degradation rate constants (T^{-1}) for the liquid and sorbed phases.

Because quinolones binding to oxide surfaces may proceed through a nonspecific and fast surface complexation reaction, such as outer-sphere or hydrogen-bound, and a specific surface complexation reaction, generally slower, such as metal-bound complexes, we assume that adsorption sites can be divided into two fractions, instantaneous (Type-1) and kinetic (Type-2) sites[44]

$$S = S_1 + S_2 \tag{3}$$

where S_1 and S_2 are solid phase concentrations associated with Type-1 and Type-2 sites, respectively. Considering Type-1 adsorption sites are always at equilibrium, S_1 can be expressed as

$$S_1 = fK\frac{C^\beta}{1 + \eta C^\beta} \tag{4}$$

The Type-2 adsorption sites are assumed to be a first-order kinetic rate process

$$\frac{\partial S_2}{\partial t} = \alpha\left[(1 - f)K\frac{C^\beta}{1 + \eta C^\beta} - S_2\right] - \mu_s S_2 \tag{5}$$

where α is a first-order kinetic rate coefficient (T^{-1}), f is the fraction of instantaneous adsorption sites (Type-1), and K, β, and η are empirical coefficients.

Transport modeling was performed with HYDRUS 1D.[43] This code allows for the numerical resolution of eqs 2-5 for several boundary and initial conditions: concentration flux at the inlet, zero concentration gradient at the outlet, and no solute at time zero. By using a least-squares optimization routine, HYDRUS 1D also allows inverse modeling to fit the model solution to the data to estimate fate and transport parameters.[43] Because of PIP transformation reactions only occurring at MnO_2 surfaces and not in solution, μ_l was set to 0. This also allows reducing the number of estimated parameters and thus avoiding nonuniqueness issues (a sensitivity analysis has been done in previous work[7]). Values for the sorption parameter K, fraction of equilibrium sites f, kinetics adsorption α, and the first-order degradation rate μ_s were determined through fitting the breakthrough curves of PIP and are reported in Table S2.

3. RESULTS AND DISCUSSION

3.1. Influence of Goethite and/or Birnessite Coating on the PIP Breakthrough. MnO_2 in MGCS columns strongly slows down PIP mobility with respect to the (MnO_2-free) GCS column (Figure 1). This can be recognized by extensive tailing of the breakthrough curve (BTC) and incomplete breakthrough of PIP in the MCS column (0.60 mg Mn/g 0.1 MCS), compared to the GCS column with a sigmoidal-shaped low-tailing BTC with total breakthrough (C/C_0 = 1) by 60 PV. In strong contrast, the 0.1 MGCS with the same Mn loading as MCS (0.60 mg Mn/g 0.1 MGCS) exhibited breakthrough at 81 PV, achieving a brief steady state

https://doi.org/10.1021/acs.est.2c05963
Environ. Sci. Technol. 2023, 57, 214−221

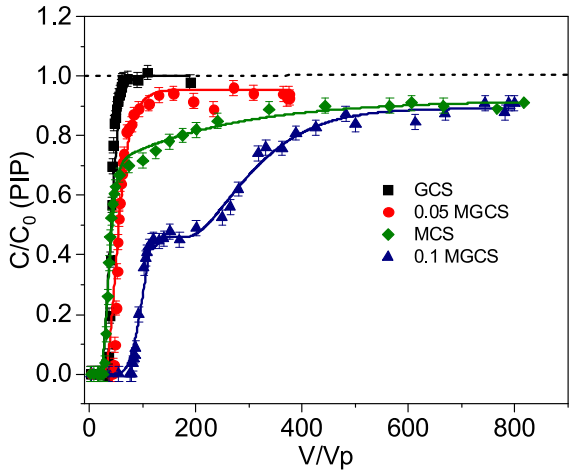

Figure 1. PIP breakthrough curve MnO_2-bearing columns (0.60 mg Mn/g MCS; 0.29 mg Mn/g 0.05 MGCS; 0.60 mg Mn/g 0.1 MGCS). The dashed line indicates the theoretical complete breakthrough of PIP (C/C_0 = 1), and solid lines are model predictions. Inflow conditions: 10 μM PIP; pH 5.2 ± 0.1; 10 mM NaCl; PV 4 mL; flow rate 0.5 mL/min. V/V_p is the ratio of the injected volume to the pore volume.

just below ~200 PV at C/C_0 ~ 0.45 and a final steady state at C/C_0 ~ 0.91, just as in MCS, after 744 PV. However, halving Mn loadings to 0.29 mg Mn/g in 0.05 MGCS produced BTC attributes intermediate to those of GCS and MCS, with the breakthrough point of PIP at 45 PV and a steady breakthrough at C/C_0 ~ 0.94 at 308 PV.

The pH of the output solution from the GCS column initially slightly decreased by ~0.4 unit but finally returned to 5.5 when a steady-state breakthrough was reached (Figure S3). However, the transformation of PIP on MnO_2 or the reductive conversion of MnO_2 released Mn(II) through

$$MnO_2 + 2e^- + 4H^+ \rightarrow Mn^{2+} + 2H_2O \quad (6)$$

As this is a proton-promoted process, the pH initially increased to 5.9 and then decreased to the initial pH value on the MCS column (Figure S3). In the MGCS column, there were no pH changes in 0.05 MGCS, while the pH followed the same behavior as for the MCS column in 0.1 MGCS (Figure S3). As PIP was mostly present in the zwitterionic form (pK_{a1} = 5.20, pK_{a2} = 6.38) (Figure S4), adsorption to goethite occurred via surface complexation reactions involving carboxylic and keto groups, with a possibility of the oxidation reaction involving the piperazine ring.[45] However, the BTC shape and the lack of byproducts in the effluent did not provide evidence for PIP oxidation by goethite. The modeling results also support the absence of PIP oxidation since no heterogeneous degradation rate (μ_s) was required to fit the BTC of PIP (Figure 1, Table S2). Conversely, modeling of the partial PIP breakthrough in the Mn-bearing MCS and MGCS columns did require μ_s (Figure 1, Table S2).

The total amount of PIP removal (by adsorption and/or oxidation) was calculated by integrating the area above the BTC of PIP. In the MCS column, the total PIP removal was ~5 μmol at ~800 PV, while the same Mn loadings in the 0.1 MGCS column removed ~11 μmol of PIP at the same breakthrough time. This consequently implies that the 0.1 MGCS column removed almost twice the amount of PIP than in the MCS column despite having the same Mn loading. As the 0.1 MGCS and GCS columns contained the same goethite loadings, the contribution of goethite in PIP removal can be estimated at ~1.5 μmol.

Enhanced MnO_2 content not only improved PIP removal in the MGCS column (3.2 μmol PIP removal in the 0.05 MGCS column vs 11 μmol in the 0.1 MGCS column) but also modified the breakthrough behavior. Indeed, a two-step behavior, two fronts and two plateaus, was observed corresponding to the pH variation during the transport experiment (Figure S3). This breakthrough behavior can be described by considering three stages, and different parameters are necessary to describe each stage of the full BTC of PIP (Table S2). If the same adsorption and oxidation parameters (i.e., α, K, f, μ_s) were used for the full BTC description, the calculated curve failed to describe the transport process of PIP, especially for the transitional plateau (Figure S5). This mobility behavior could be explained by the pH impact on the heterogeneous redox reaction and/or (re)adsorption of redox products. It has been reported that fluoroquinolone binding to negatively charged Mn-oxide surfaces proceeds through a heterogeneous redox reaction, whereby two one-electron transfers or a single two-electron transfer oxidizes PIP and reduces surface-bound metal sites.[17,19,46] This will be investigated in the next section.

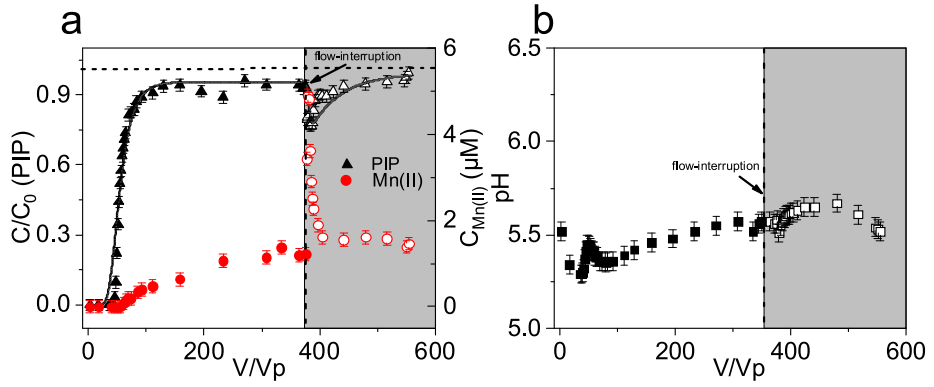

Figure 2. Breakthrough curves of a) PIP and Mn(II) and b) pH in the 0.05 MGCS column. The horizontal dashed line indicates the theoretical complete breakthrough of PIP (C/C_0 = 1), and solid lines are model predictions. The vertical dashed lines indicate the moment of flow interruption (duration 24 h). The empty symbols in the shadow area indicate the second stage after flow resumption. Inflow conditions: 10 μM PIP; pH 5.2 ± 0.1; 10 mM NaCl; PV 4 mL; flow rate 0.5 mL/min. V/V_p is the ratio of the injected volume to the pore volume.

https://doi.org/10.1021/acs.est.2c05963
Environ. Sci. Technol. 2023, 57, 214−221

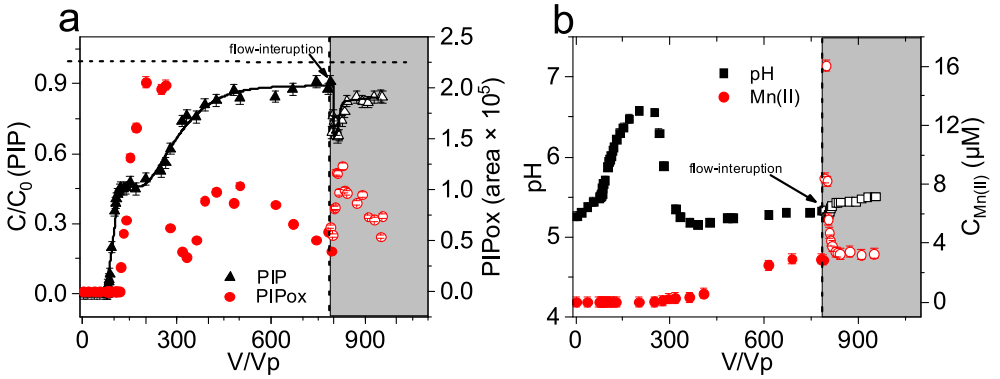

Figure 3. Breakthrough curves of (a) PIP and PIP_{ox} (peak area of the PIP byproduct; M-26) and (b) Mn(II), pH in the 0.1 MGCS column. The horizontal dashed line indicates the theoretical complete breakthrough of PIP (C/C_0 = 1), and solid lines are model predictions. The vertical dashed lines indicate the moment of flow interruption (duration 24 h). The empty symbols in the shadow area indicate the second stage after flow resumption. Inflow conditions: 10 μM PIP; pH 5.2 ± 0.1; 10 mM NaCl; PV 4 mL; flow rate 0.5 mL/min. V/V_p is the ratio of the injected volume to the pore volume.

3.2. Impact of Manganese Oxide Content on PIP Oxidation in Columns. To further investigate PIP transport in MGCS columns, redox byproducts (dissolved Mn(II) and the oxidized byproduct of PIP) were monitored in the outflow solution throughout the breakthrough experiment and upon flow interruption. Our flow/no flow/flow sequence protocol allowed us to check kinetic limitations through determination of the BTC of species before interruption and after resumption of flow.

In the 0.05 MGCS column, Mn(II) was detected in the effluent solution at the same time as PIP and then reached a steady-state concentration of 1.2 μM. Increasing the residence time of PIP in the 0.05 MGCS column by interrupting the flow for 24 h (376 PV) did not influence the incomplete breakthrough as the same partial breakthrough (C/C_0 = 0.94) was still observed upon flow resumption (Figure 2a). This flow interruption period allowed species to react over a longer period during flow-through conditions. Here, relative concentrations of PIP dropped from 0.94 to 0.76, while those of Mn(II) increased sharply from 1.2 to 5 μM; yet, solution pH values were stable throughout the course of the experiment (Figure 2b). This behavior pointed to rate-limited sorption/redox processes from co-occurring adsorption reactions and heterogeneous redox reactions. Note that BTC curves in separate bromide tracer experiments did not change following a flow/no-flow/flow sequence, thereby excluding the possibility of physical nonequilibrium or diffusive mass transfer that might cause changes in PIP and Mn(II) concentrations. Upon flow resumption, both PIP and Mn(II) concentrations reached the steady-state concentrations prior to the stop-flow. Although Mn(II) was detected by ICP-AES as the reduced byproduct, no oxidized byproduct of PIP (hereafter referred as PIP_{ox}) was detected in the effluent throughout the course of the experiment (Figure 2a). This could be explained by the very low concentrations of generated redox products and/or strong binding to minerals at the working pH value (5.2).

In the 0.1 MGCS column, redox products (Mn(II) and PIP_{ox}) were detected throughout the course of the experiment (Figure 3a). LC/MS analysis confirmed the PIP_{ox} had a m/z value of 227 (M-26), formed through N-dealkylation of the piperazine ring of PIP (Figure S6). As previously observed for quinolone compounds,[17,19] one electron is transferred from the sorbed compound to the surface-bound Mn^{IV}, yielding radical intermediates, and Mn^{III} that can be further reduced to give Mn^{II} as follows:

$$\equiv Mn^{IV} + PIP \rightarrow \equiv Mn^{IV} - PIP_{ad} \rightarrow \equiv Mn^{III}/Mn^{II} - PIP^{+} \rightarrow Mn^{II} + PIP_{ox} \quad (7)$$

As seen in Figure 3a, PIP_{ox} concentration in the effluent solution reached its maximum and then decreased after ~175 PV. Prior to flow-interruption, the BTC of PIP_{ox} followed the outflow pH values, as PIP_{ox} binding to minerals is pH-dependent. However, the peak area of the LC/MS data corresponding to PIP_{ox} was not constant (no steady-state values) during the course of the experiment. Increasing the residence in the column with flow-interruption, decreased PIP concentration but increased that of PIP_{ox}. When the flow was resumed, PIP concentration reached again a plateau, with a steady-state value lower than that before flow interruption (0.9 to 0.8). High MnO_2 content exhibited greater removal ability of PIP and more Mn(II) generation. For example, a higher k value, first-order degradation rate coefficient (including sorption and oxidation) was obtained in the 0.1 MGCS (k = 2.1×10^{-4} min^{-1}) compared to 0.05 MGCS (k = 1.4×10^{-4} min^{-1}) by

$$k = -\frac{In\left(\frac{C_a}{C_b}\right)}{t} \quad (8)$$

Here, C is the PIP effluent concentration before (C_b) and after (C_a) flow-interruption, and t is the duration of interruption (24 h).

The shape of the breakthrough curve of Mn(II) in the 0.1 MGCS column was similar to that of the 0.05 MGCS column. However, Mn(II) did not exhibit breakthrough with PIP (as the 0.05 MGCS column) and was only detected after injection of ~300 PV. This delayed Mn(II) breakthrough corresponds to an increase in the outflow pH value (see Figure 3b) and thus can be explained by the increase in Mn(II) binding onto goethite with an increasing pH (see batch data in Figure S7). The effluent concentration of Mn(II) thereafter reached a plateau-like, steady-state value when the pH decreased to the inflow pH (~5.2). In MCS, no Mn(II) desorbed into the effluent solution (Figure S8). The presence of dissolved Mn(II) in outflow solutions of MGCS columns (0 μM in the MCS column vs. 2.5 μM in the 0.1 MGCS column at pH 5.2)

https://doi.org/10.1021/acs.est.2c05963
Environ. Sci. Technol. 2023, 57, 214−221

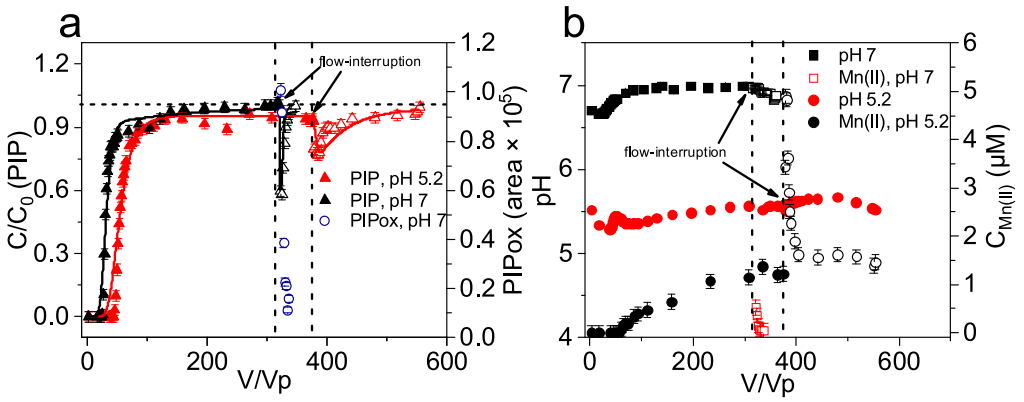

Figure 4. Breakthrough curves of (a) PIP and PIP_{ox} (peak area of PIP byproduct; M-26) and (b) Mn(II), pH on different pH's in the 0.05 MGCS column. The horizontal dashed line indicates the theoretical complete breakthrough of PIP ($C/C_0 = 1$), and solid lines are model predictions. The vertical dashed lines indicate the moment of flow interruption (duration 24 h). The empty symbols indicate the second stage after flow resumption. Inflow conditions: 10 μM PIP, pH 5.2 ± 0.1 and 7.0 ± 0.1, 10 mM NaCl, PV 4 mL, flow rate 0.5 mL/min. V/V_p is the ratio of the injected volume to the pore volume.

suggests that the presence of goethite altered the Mn(II) uptake by MnO_2 at this pH value and thus increased its mobility through the column system. This was confirmed further by Mn(II) batch adsorption data on MCS and MGCS (Figure S9), where 70% of dissolved Mn(II) was removed by MCS, while only 40% was removed with MGCS under the same experimental conditions (see Figure S9). Additional batch experiments showed that PIP was continuously removed (sorption + oxidation) by MGCS, yet only Mn(II) (no PIP_{ox}) was detected in the solution (Figure S10). As observed in the column system, the presence of goethite likely ensured preferential adsorption of PIP or PIP_{ox} over Mn(II) onto MGCS at pH 5.2. This aligns with our batch adsorption tests (Figure S7) revealing strong PIP and weak Mn(II) loadings at this pH value. PIP binding was also lower and Mn(II) binding was greater at a larger pH, even with competitive sorption at pH > 6. Taken together, these findings confirmed that interactions between positively charged goethite (PZC 9.1) and negatively charge MnO_2 (PZC 2.4) particles decreased overall cation adsorption in the MGCS system. As a result, dissolved Mn(II) ion was flushed out of the column, thus preventing further interactions with MnO_2 and mitigating surface passivation, which is generally observed in MnO_2-based redox reactions (e.g., as in MCS column).[4,17,42] Indeed, it has been reported that Mn(II) binding at the MnO_2 surface may decrease the oxidation rate of organic compounds because (i) Mn(II) may block redox reactive sites on the oxide surface, preventing adsorption of the organic compound or competitively reacting with MnO_2, and (ii) surface bound Mn(II) may decrease the average oxidation state of MnO_2 and therefore slow the rate of electron transfer.[4,17,42,46] This may explain the higher reactivity of the MGCS system in total PIP removal with respect to MCS.

3.3. PIP Transport at Two pH Values. An additional PIP breakthrough experiment in the 0.05 MGCS column was repeated but at pH 7.0. In contrast to experiments at pH 5.2 (Figure 4), no variations in pH occurred. Only 1.8 μmol of PIP was removed at neutral pH, compared to that at pH 5.2 (3.2 μmol), because acidic conditions favored PIP oxidation and adsorption onto MnO_2 and/or goethite. A steeper BTC and earlier breakthrough point, with complete breakthrough, were achieved, whereas no PIP_{ox} or Mn(II) was detected in the column effluent, indicating extreme low or no PIP transformation occurred at pH 7. This observation is consistent with our modeling result since setting $\mu_s = 0$ can well fit the BTC of PIP at pH 7 (Table S2).

No oxidation occurred during the first stage, but when the residence time is increased, Mn(II) and PIP_{ox} were detected upon flow resumption. The PIP relative concentration drops to 0.6 at pH 7 but only to 0.8 at pH 5.2 when the flow was resumed (Figure 4a). According to eq 8, more PIP was removed, and a higher k value was obtained during the flow interruption period at pH 7 (1.4×10^{-4} min^{-1} at pH 5.2, 3.5×10^{-4} min^{-1} at pH 7, Table S3). As only sorption happened in the first step, we suppose that the pristine MnO_2 surfaces may enable more PIP oxidation during the flow interruption period. Furthermore, less MnO_2 passivation can be expected, as more Mn(II) can be adsorbed by goethite at pH 7 (see batch data in Figure S7).

In summary, both experimental and modeling results show that binary mixtures of manganese oxides and goethite are capable of oxidizing and removing PIP more efficiently than in the single phase. MGCS may overcome the major drawbacks of MCS to be used as a potential geomedia for antibiotic removal. Indeed, preferential adsorption of Mn(II) on negatively charged MnO_2 and the progressive buildup of Mn(II) in the column decreased the reactivity of the MCS column over breakthrough time. However, MGCS preferential adsorbed PIP or PIP_{ox} over Mn(II) and thereby reduced the passivation effect by dissolved Mn(II).

4. ENVIRONMENTAL SIGNIFICANCE

This study contributed to mounting evidence that the environmental fate of pollutants cannot be predicted based on the sorption/oxidation data of single minerals. A thorough examination of the redox reactivity within complex mineral assemblages under both batch and continuous flow conditions is necessary for an accurate assessment of contaminant transport in natural environments (e.g., soils and sediments) or engineered infiltration systems (e.g., MAR). Here, we showed that coexisting minerals, in our case goethite, can alter the overall reactivity of the redox-active MnO_2. In particular, interactions between the positively charged goethite and the negatively charged MnO_2 particles decreased Mn(II) surface loadings, thus facilitating its mobility through the column. In addition to advancing ideas on environmental processes,

https://doi.org/10.1021/acs.est.2c05963
Environ. Sci. Technol. 2023, 57, 214−221

knowledge that goethite-MnO_2 interactions decrease MnO_2 passivation could be used to design novel geomedia filters. Fe and Mn binary oxides may overcome the major drawbacks of Mn-oxides to be used as a potential geomedia filter for antibiotic removal. As manganese oxides have the potential to be applied as a filter to prevent organic contaminants from percolating into the groundwater sources in both natural soils and artificial infiltration systems, this work could help in designing efficient geomedia in treatment technologies (industrial and/or municipal wastewater, agricultural runoff, stormwater, etc.). Those contaminated systems contain diverse organic groups such as pharmaceuticals and personal care products, pesticides, and detergents, with varying concentrations. Therefore, the amount MnO_2 and/or goethite coated on sand should be optimized to further enhance the reactivity and longevity of geomedia and prior to the application of GMCS in infiltration systems. Finally, as Fe- and Mn-oxides may coexist with each other as particulate coatings, the transport model developed here will help in understanding fate and transformation of emerging compounds in natural environments such as soils and sediments.

■ ASSOCIATED CONTENT

Supporting Information

The Supporting Information is available free of charge at https://pubs.acs.org/doi/10.1021/acs.est.2c05963.

Synthesis of minerals and coatings materials; pH dependent PIP and Mn(II) adsorption onto GCS; kinetics of PIP removal with 0.05 GMCS; kinetic sorption of Mn(II) on MCS and 0.05 GMCS; PIP and PIP_{ox} detection methods; SEM images of GCS, 0.05 MGCS, and 0.1 MGCS; Br^- transport experiments; breakthrough curves of pH in different MnO_2 content packed columns; chemical speciation of PIP; modeling of PIP transport; PIP and identified oxidation byproduct (PIPox) by LC/MS; PIP and Mn(II) removal under different pH's; byproduct identification in MCS column; kinetic Mn(II) adsorption on MCS or MGCS; changes in PIP and Mn(II) concentrations; experimental conditions and results for dynamic column breakthrough experiments; parameters of PIP transport under flow-through conditions; and degradation rate coefficient (PDF)

■ AUTHOR INFORMATION

Corresponding Author

Khalil Hanna − *Université de Rennes, Ecole Nationale Supérieure de Chimie de Rennes, CNRS, ISCR-UMR 6226, F-35000 Rennes, France; Institut Universitaire de France (IUF), MESRI, 1 rue Descartes, 75231 Paris, France;* orcid.org/0000-0002-6072-1294; Phone: +33 2 23 23 80 27; Email: khalil.hanna@ensc-rennes.fr

Authors

Tao Luo − *Université de Rennes, Ecole Nationale Supérieure de Chimie de Rennes, CNRS, ISCR-UMR 6226, F-35000 Rennes, France; Department of Chemistry, Umeå University, Umeå SE-901 87, Sweden*

Rasesh Pokharel − *Department of Earth Sciences, Copernicus Institute of Sustainable Development, Faculty of Geosciences, Utrecht University, 3584 CB Utrecht, Netherlands;* orcid.org/0000-0003-1889-2433

Tao Chen − *Université de Rennes, Ecole Nationale Supérieure de Chimie de Rennes, CNRS, ISCR-UMR 6226, F-35000 Rennes, France*

Jean-François Boily − *Department of Chemistry, Umeå University, Umeå SE-901 87, Sweden;* orcid.org/0000-0003-4954-6461

Complete contact information is available at: https://pubs.acs.org/10.1021/acs.est.2c05963

Author Contributions

T.L. and R.P. contributed equally to this work.

Notes

The authors declare no competing financial interest.

■ ACKNOWLEDGMENTS

The authors acknowledge the support of the Institut Universitaire de France, the Swedish Research Council (2020-04853), the French National Research Agency via the INFLOW project (ANR-21-CE29-0008-01), and the CNRS (IEA 2018-2020). We also thank the China Scholarship Council for a Ph.D. grant and Région Bretagne for a mobility grant for an extended research stay at Umeå University.

■ REFERENCES

(1) Post, J. E. Manganese Oxide Minerals: Crystal Structures and Economic and Environmental Significance. *Proc. Natl. Acad. Sci. U. S. A.* **1999**, *96* (7), 3447−3454.

(2) Cornell, R. M.; Schwertmann, U.*The Iron Oxides: Structure, Properties, Reactions, Occurrences and Uses*; Wiley-vch: Weinheim, 2003; DOI: 10.1002/3527602097.

(3) Lion, L. W.; Altmann, R. S.; Leckie, J. O. Trace-Metal Adsorption Characteristics of Estuarine Particulate Matter: Evaluation of Contributions of Fe/Mn Oxide and Organic Surface Coatings. *Environ. Sci. Technol.* **1982**, *16* (10), 660−666.

(4) Remucal, C. K.; Ginder-Vogel, M. A Critical Review of the Reactivity of Manganese Oxides with Organic Contaminants. *Environ. Sci. Process. Impacts* **2014**, *16* (6), 1247−1266.

(5) Li, J.; Zhao, L.; Zhang, R.; Teng, H. H.; Padhye, L. P.; Sun, P. Transformation of Tetracycline Antibiotics with Goethite: Mechanism, Kinetic Modeling and Toxicity Evaluation. *Water Res.* **2021**, *199*, 117196.

(6) Huang, X.; Chen, Y.; Walter, E.; Zong, M.; Wang, Y.; Zhang, X.; Qafoku, O.; Wang, Z.; Rosso, K. M. Facet-Specific Photocatalytic Degradation of Organics by Heterogeneous Fenton Chemistry on Hematite Nanoparticles. *Environ. Sci. Technol.* **2019**, *53* (17), 10197−10207.

(7) Zhou, L.; Martin, S.; Cheng, W.; Lassabatere, L.; Boily, J. F.; Hanna, K. Water Flow Variability Affects Adsorption and Oxidation of Ciprofloxacin onto Hematite. *Environ. Sci. Technol.* **2019**, *53* (17), 10102−10109.

(8) Chen, Y.; Lu, X.; Liu, L.; Wan, D.; Chen, H.; Zhou, D.; Sharma, V. K. Oxidation of B-Blockers by Birnessite: Kinetics, Mechanism and Effect of Metal Ions. *Chemosphere* **2018**, *194*, 588−594.

(9) Liang, M.; Xu, S.; Zhu, Y.; Chen, X.; Deng, Z.; Yan, L.; He, H. Preparation and Characterization of Fe-Mn Binary Oxide/Mulberry Stem Biochar Composite Adsorbent and Adsorption of Cr(VI) from Aqueous Solution. *Int. J. Environ. Res. Public Health* **2020**, *17*, 676.

(10) Ricko, A. N.; Psoras, A. W.; Sivey, J. D. Reductive Transformations of Dichloroacetamide Safeners: Effects of Agrochemical Co-Formulants and Iron Oxide + Manganese Oxide Binary-Mineral Systems. *Environ. Sci. Process. Impacts* **2020**, *22* (10), 2104−2116.

(11) Zhang, G.; Liu, F.; Liu, H.; Qu, J.; Liu, R. Respective Role of Fe and Mn Oxide Contents for Arsenic Sorption in Iron and Manganese Binary Oxide: An X-Ray Absorption Spectroscopy Investigation. *Environ. Sci. Technol.* **2014**, *48* (17), 10316−10322.

(12) Liu, H.; Chen, T.; Frost, R. L. An Overview of the Role of Goethite Surfaces in the Environment. *Chemosphere* **2014**, *103*, 1−11.
(13) Evanko, C. R.; Dzombak, D. A. Surface Complexation Modeling of Organic Acid Sorption to Goethite. *J. Colloid Interface Sci.* **1999**, *214*, 189−206.
(14) Cheng, W.; Zhou, L.; Marsac, R.; Boily, J. F.; Hanna, K. Effects of Organic Matter-Goethite Interactions on Reactive Transport of Nalidixic Acid: Column Study and Modeling. *Environ. Res.* **2020**, *191*, 110187.
(15) Wang, L.; Cheng, H. Birnessite (γ-MnO_2) Mediated Degradation of Organoarsenic Feed Additive p-Arsanilic Acid. *Environ. Sci. Technol.* **2015**, *49* (6), 3473−3481.
(16) Zhao, W.; Tan, W.; Wang, M.; Xiong, J.; Liu, F.; Weng, L.; Koopal, L. K. CD-MUSIC-EDL Modeling of Pb^{2+} Adsorption on Birnessites: Role of Vacant and Edge Sites. *Environ. Sci. Technol.* **2018**, *52* (18), 10522−10531.
(17) Pokharel, R.; Li, Q.; Zhou, L.; Hanna, K. Water Flow and Dissolved Mn(II) Alter Transformation of Pipemidic Acid by Manganese Oxide. *Environ. Sci. Technol.* **2020**, *54* (13), 8051−8060.
(18) Hanna, K.; Boily, J. F. Sorption of Two Naphthoic Acids to Goethite Surface under Flow through Conditions. *Environ. Sci. Technol.* **2010**, *44* (23), 8863−8869.
(19) Zhang, H.; Huang, C. H. Oxidative Transformation of Fluoroquinolone Antibacterial Agents and Structurally Related Amines by Manganese Oxide. *Environ. Sci. Technol.* **2005**, *39* (12), 4474−4483.
(20) Wang, A.; Wang, H.; Deng, H.; Wang, S.; Shi, W.; Yi, Z.; Qiu, R.; Yan, K. Controllable Synthesis of Mesoporous Manganese Oxide Microsphere Efficient for Photo-Fenton-like Removal of Fluoroquinolone Antibiotics. *Appl. Catal. B Environ.* **2019**, *248* (July2018), 298−308.
(21) Cheng, W.; Kalahroodi, E. L.; Marsac, R.; Hanna, K. Adsorption of Quinolone Antibiotics to Goethite under Seawater Conditions: Application of a Surface Complexation Model. *Environ. Sci. Technol.* **2019**, *53*, 1130−1138.
(22) Anderson, P. R.; Benjamin, M. M. Surface and Bulk Characteristics of Binary Oxide Suspensions. *Environ. Sci. Technol.* **1990**, *24* (5), 692−698.
(23) Anderson, P. R.; Benjamin, M. M. Modeling Adsorption in Aluminum-Iron Binary Oxide Suspensions. *Environ. Sci. Technol.* **1990**, *24* (10), 1586−1592.
(24) Meng, X.; Letterman, R. D. Effect of Component Oxide Interaction on the Adsorption Properties of Mixed Oxides. *Environ. Sci. Technol.* **1993**, *27* (5), 970−975.
(25) Taujale, S.; Zhang, H. Impact of Interactions between Metal Oxides to Oxidative Reactivity of Manganese Dioxide. *Environ. Sci. Technol.* **2012**, *46*, 2764−2771.
(26) Zhang, H.; Taujale, S.; Huang, J.; Lee, G. Effects of NOM on Oxidative Reactivity of Manganese Dioxide in Binary Oxide Mixtures with Goethite or Hematite. *Langmuir* **2015**, *31*, 2790−2799.
(27) Huang, J.; Zhang, H. Redox Reactions of Iron and Manganese Oxides in Complex Systems. *Front. Environ. Sci. Eng.* **2020**, *14* (5), 76.
(28) Shimizu, M.; Nakamura, S.; Kurobe, N.; Takase, Y. Absorption, Distribution, and Excretion of Pipemidic Acid. *Antimicrob Agents Chemother* **1975**, *7*, 441−446.
(29) Golet, E. M.; Alder, A. C.; Giger, W. Environmental Exposure and Risk Assessment of Fluoroquinolone Antibacterial Agents in Wastewater and River Water of the Glatt Valley Watershed, Switzerland. *Environ. Sci. Technol.* **2002**, *36* (17), 3645−3651.
(30) Kolpin, D. W.; Furlong, E. T.; Meyer, M. T.; Thurman, E. M.; Zaugg, S. D.; Barber, L. B.; Buxton, H. T. Pharmaceuticals, Hormones, and Other Organic Wastewater Contaminants in U.S. Streams, 1999−2000: A National Reconnaissance. *Environ. Sci. Technol.* **2002**, *36* (18), 1202−1211.
(31) Hartmann, A.; Golet, E. M.; Gartiser, S.; Alder, A. C.; Koller, T.; Widmer, R. M. Primary DNA Damage but Not Mutagenicity Correlates with Ciprofloxacin Concentrations in German Hospital Wastewaters. *Arch. Environ. Contam. Toxicol.* **1999**, *36* (2), 115−119.
(32) Weist, K.; Högberg, L. D. ECDC Publishes 2015 Surveillance Data on Antimicrobial Resistance and Antimicrobial Consumption in Europe. *Eurosurveillance* **2016**, *21*, 30401.
(33) Ma, Y.; Li, M.; Wu, M.; Li, Z.; Liu, X. Occurrences and Regional Distributions of 20 Antibiotics in Water Bodies during Groundwater Recharge. *Sci. Total Environ.* **2015**, *518*−*519*, 498−506.
(34) Manyi-Loh, C.; Mamphweli, S.; Meyer, E.; Okoh, A. Antibiotic Use in Agriculture and Its Consequential Resistance in Environmental Sources: Potential Public Health Implications. *Molecules* **2018**, *23*, 795.
(35) Sposito, G.*The Surface Chemistry of Soils*; Oxford University Press: 1984.
(36) Zhou, L.; Cheng, W.; Marsac, R.; Boily, J. F.; Hanna, K. Silicate Surface Coverage Controls Quinolone Transport in Saturated Porous Media. *J. Colloid Interface Sci.* **2022**, *607*, 347−356.
(37) McKenzie, R. M. The Synthesis of Birnessite, Cryptomelane, and Some Other Oxides and Hydroxides of Manganese. *Miner. Mag.* **1971**, *38*, 493−502.
(38) Gaboriaud, F.; Ehrhardt, J. J. Effects of Different Crystal Faces on the Surface Charge of Colloidal Goethite (α-FeOOH) Particles: An Experimental and Modeling Study. *Geochim. Cosmochim. Acta* **2003**, *67* (5), 967−983.
(39) Hanna, K.; Martin, S.; Quilès, F.; Boily, J.-F. Sorption of Phthalic Acid at Goethite Surfaces under Flow-Through Conditions. *Langmuir* **2014**, *30* (23), 6800−6807.
(40) Rusch, B.; Hanna, K.; Humbert, B. Coating of Quartz Silica with Iron Oxides: Characterization and Surface Reactivity of Iron Coating Phases. *Colloids Surfaces A Physicochem. Eng. Asp.* **2010**, *353* (2−3), 172−180.
(41) Stumm, W.*Chemistry of the Solid-Water Interface: Processes at the Mineral-Water and Particle-Water Interface in Natural Systems*; John Wiley & Sons Inc.: 1992.
(42) Charbonnet, J. A.; Duan, Y.; Van Genuchten, C. M.; Sedlak, D. L. Chemical Regeneration of Manganese Oxide-Coated Sand for Oxidation of Organic Stormwater Contaminants. *Environ. Sci. Technol.* **2018**, *52* (18), 10728−10736.
(43) Šimůnek, J.; van Genuchten, M. T. Modeling Nonequilibrium Flow and Transport Processes Using HYDRUS. *Vadose Zo. J.* **2008**, *7* (2), 782−797.
(44) Van Genuchten, M. T.; Wagenet, R. J. Two-Site/Two-Region Models for Pesticide Transport and Degradation: Theoretical Development and Analytical Solutions. *Soil Sci. Soc. Am. J.* **1989**, *53* (5), 1303−1310.
(45) Zhang, H.; Huang, C. H. Adsorption and Oxidation of Fluoroquinolone Antibacterial Agents and Structurally Related Amines with Goethite. *Chemosphere* **2007**, *66* (8), 1502−1512.
(46) Li, Q.; Pokharel, R.; Zhou, L.; Pasturel, M.; Hanna, K. Coupled Effects of Mn(II), pH and Anionic Ligands on the Reactivity of Nanostructured Birnessite. *Environ. Sci. Nano* **2020**, *7* (12), 4022−4031.

https://doi.org/10.1021/acs.est.2c05963
Environ. Sci. Technol. 2023, 57, 214−221